

Computational characterization of bulk heterojunction nanomorphology

Olga Wodo, Srikanta Tirthapura, Sumit Chaudhary, and Baskar Ganapathysubramanian

Citation: *J. Appl. Phys.* **112**, 064316 (2012); doi: 10.1063/1.4752864

View online: <http://dx.doi.org/10.1063/1.4752864>

View Table of Contents: <http://jap.aip.org/resource/1/JAPIAU/v112/i6>

Published by the [American Institute of Physics](#).

Related Articles

High efficiency and high photo-stability zinc-phthalocyanine based planar heterojunction solar cells with a double interfacial layer

Appl. Phys. Lett. **101**, 113301 (2012)

High efficiency and high photo-stability zinc-phthalocyanine based planar heterojunction solar cells with a double interfacial layer

APL: Org. Electron. Photonics **5**, 207 (2012)

Theory and simulation of organic solar cell model compounds: How packing and morphology determine the electronic conductivity

J. Chem. Phys. **137**, 094903 (2012)

Simulated annealing electro-photonic optimization of organic solar cells

J. Appl. Phys. **112**, 054502 (2012)

Sheaf-like-ZnO@Ag nanocomposite materials modified photoanode for low-cost metal-free organic dye-sensitized solid-state solar cells

Appl. Phys. Lett. **101**, 093112 (2012)

Additional information on *J. Appl. Phys.*


Journal Homepage: <http://jap.aip.org/>

Journal Information: http://jap.aip.org/about/about_the_journal

Top downloads: http://jap.aip.org/features/most_downloaded

Information for Authors: <http://jap.aip.org/authors>

ADVERTISEMENT



Special Topic Section:
PHYSICS OF CANCER

Why cancer? Why physics? [View Articles Now](#)

Computational characterization of bulk heterojunction nanomorphology

Olga Wodo,¹ Srikanta Tirthapura,² Sumit Chaudhary,^{2,3,a)}
and Baskar Ganapathysubramanian^{1,2,b)}

¹Department of Mechanical Engineering, Iowa State University, Ames, IA, 50011 USA

²Department of Electrical and Computer Engineering, Iowa State University, Ames, IA, 50011 USA

³Department of Materials Science and Engineering, Iowa State University, Ames, IA, 50011 USA

(Received 27 January 2012; accepted 9 August 2012; published online 20 September 2012)

The bulk heterojunction (BHJ) nanomorphology in organic solar cells strongly affects the final efficiency of the device. Progress in experimental techniques now allows visualization of the complex 3D BHJ morphology. It is, therefore, important to characterize the topological properties of the morphology in order to quantify the link between morphology features and performance. Here, we introduce a suite of morphology descriptors which encode the complex nature of the multi-stage photovoltaic process in the BHJ. These morphology descriptors are easily determined using an approach based on converting the morphology into an equivalent weighted, labeled, undirected graph. We show how these descriptors can be used to interrogate BHJ morphologies, allow identification of bottlenecks in the photovoltaic process, and conduct quantitative comparison between morphologies with respect to each sub-process in the photovoltaic phenomena. This framework provides a simple and easy-to-use characterization tool that can be used to unravel the impact of morphology on complex transport phenomena. © 2012 American Institute of Physics. [<http://dx.doi.org/10.1063/1.4752864>]

I. INTRODUCTION

Modern organic solar cells (OSCs) have a so-called bulk-heterojunction (BHJ) architecture,^{1–3} in which the photovoltaic active-layer is a well-mixed blend of two types of materials. One type is electron donating while the other is electron accepting. The nanomorphology of a BHJ thin film is of great importance for OSCs due to its enormous influence on the final efficiency of the device.^{4,5} Recent advances in microscopy (electron tomography,⁶ EF TEM⁷) now allow accurate, highly resolved, three-dimensional visualization of the structure of BHJ. These data-sets are usually very large, and visual inspection and interpretation are invariably unproductive and very time-consuming. This naturally brings up the necessity of efficiently performing morphology characterization, where the complex BHJ-morphology can be reduced to a set of physically meaningful morphology descriptors. These descriptors can then be used for quantitative, predictive assessment of device performance. Such an approach facilitates linking fabrication process with morphology, as well as morphology with the final properties of the device. In particular, it would be important to identify morphology features/descriptors that are crucial and correlated with the performance. Then, the objective of linking process with structure is to find fabrication conditions that lead to these desired morphological features. This is pressing research question where several important results have been recently reported.^{8–11}

In this work, we formulate a broad suite of morphology descriptors that quantify morphological features with respect to each sub-process in the photo-voltaic process. These

descriptors are constructed in a very efficient manner by posing the problem of construction of morphology descriptors into a problem involving graph characterization, where several scalable, linear complexity algorithms exist. We illustrate this framework by comprehensively characterizing several representative BHJ morphologies.

Morphology characterization has been a subject of previous studies. Descriptors, such as autocorrelation function (ACF),^{12,13} interfacial length,^{14,15} and fraction of domain connected to given electrode¹⁶ have been used to characterize the morphology. These quantities give important insight into physics by extracting coarse scale information. Nevertheless, they lack comprehensiveness and miss some important, finer-scale aspects of the underlying physics. For example, the ACF only provides the averaged feature size of the morphology. The averaged domain size is a rough estimate of the distance excitons need to diffuse to reach the interface. However, the ACF does not reveal the *actual fraction* of the domain that can potentially contribute to exciton dissociation. In addition, none of these descriptors give insight into the tortuosity of paths, which affects charge transport.

II. PHYSICALLY MEANINGFUL MORPHOLOGY DESCRIPTORS

We start this analysis by enumerating the effects of morphology on each stage of the photo-voltaic process. We enumerate each stage within the OSC photovoltaic process and its relationship to morphology. This provides intuitive guidelines on the choice of descriptors. We assume that morphology consists of two phases: donor-rich phase (D) and acceptor-rich phase (A).²⁶

1. Light absorption leads to exciton (bound pair of electron and hole) generation. Useful exciton generation mostly occurs *only in the D-material*.

^{a)}Also at Department of Materials Science and Engineering, Iowa State University, Ames, Iowa, 50011, USA.

^{b)}Electronic mail: baskarg@iastate.edu. URL: <http://www3.me.iastate.edu/bglab/>.

2. The exciton has a *finite lifetime* to diffuse within *D-material*.
3. Only excitons that reach the *D-A interface* separate into free charges.
4. Electrons travel *only via paths consisting of A-material* to be collected at cathode, while holes travel *only via paths consisting of D-material* to be collected at anode.

The failure to convert photons into current can occur at any stage. For instance, if an exciton does not reach the interface (due to its limited life time), the electron-hole pair undergoes radiative or non-radiative recombination. Similarly, if dissociated charges do not reach the electrodes, they also undergo bimolecular or trap-assisted recombination or both.

Based on this analysis and taking into account the multi-stage nature of the photovoltaic process in a BHJ OSC, motivates us to formulate and categorize three groups of morphology descriptors: morphology descriptors quantifying light absorption, exciton dissociation, and charge transport (enumerated in Table I).

1. Quantifying light absorption

In most OSC, only one type of material (D-material) absorbs light to generate excitons. The distribution of donor within active layer as well as the variation of light intensity affects the amount of light absorbed. It has been shown that the exciton generation rate depends on the thickness of the film.^{17,18} A natural descriptor to quantify light absorption is therefore the fraction of D material, f_{abs} , within the active-layer. Additionally, to account for the intensity change along film depth, each point of the D-material is weighted by the normalized light intensity at that location. We call this weighted fraction of D-material, f_{w-abs} .

2. Quantifying exciton dissociation

An exciton has a very short lifetime, during which it must reach the D-A interface to be useful. It can only diffuse a finite distance compatible with the exciton diffusion length, L_d . Therefore, to enhance exciton harvesting, the distance

from D-material to the D-A interface should be shorter than L_d . Moreover, D-A interfacial area should be maximized to ensure increased exciton dissociation. Therefore, a natural descriptor is the shortest distance from any D-material point to the D-A interface. A cumulative histogram of such distances concisely describes exciton diffusion/dissociation. The value of the cumulative histogram at a distance d is the fraction of the D-material that is within this distance to the interface. In this way, the fraction, $f_{diss}^{L_d}$, of D-material within L_d from the D-A interface can be determined. Furthermore, the probability of an exciton reaching the D-A interface depends on the distance it needs to travel. To account for this factor, we introduce a weighting function, $f(d)$, that expresses the probability of reaching an interface by the exciton generated at distance d (this probability can be expressed as $f(d) = \exp(-d/L_d)$).^{19,20} We use this function to construct the weighted histogram of distances from D-material to the D-A interface. The weighted fraction, f_{w-diss} , of D-material can be estimated from the cumulative weighted histogram. The interfacial area, I , is the second natural descriptor reflecting the nature of exciton dissociation.

3. Quantifying charge transport

To improve hole transport and extraction, all D-material should be connected to anode, preferably with short and straight paths. Similarly, to improve electron transport and extraction, all A-material should be connected to cathode, preferably with short and straight paths. Moreover, charge transport is a complementary process. That is, charges separated at the interface should both be able to reach the electrodes via respective paths. It follows that the morphology should consist of complementary paths. Finally, morphology should consist of balanced paths to avoid charge accumulation. That is, the electron and hole path lengths should be balanced. To characterize morphology with respect to these features of charge transport, we construct four morphology descriptors:

1. To quantify the regions of the morphology useful for charge-transport, we determine the fraction, f_{conn}^D , of D-material connected to anode, the fraction, f_{conn}^A , of

TABLE I. List of morphology descriptors with their physical background.

Stage	Morphology descriptor	Physical background
Light absorption	f_{abs} —fraction of light absorbing material	Only D-material absorbs light
	f_{w-abs} —weighted fraction of light absorbing material	Intensity of light changes along depth from the top surface
Exciton dissociation	$f_{diss}^{L_d}$ —fraction of D-material within distance L_d to the interface	Limited lifetime of exciton, only these excitons created in distance shorter than exciton diffusion length have high chance to reach interface
	f_{w-diss} —weighted fraction of D-material	Function $f(d)$ weights shorter distances with higher probability of reaching the interface, while longer distances are associated with lower probability
Charge transport	I —interfacial area	Only at the D-A interface exciton dissociates into free charges
	f_{out}^{conn} —fraction of useful domains	Only regions with direct connection to relevant electrode constitute pathways for charges to travel
	f_{out}^{path} —fraction of interface with both paths to electrodes	Charge transport is a complementary process
	f_{out}^{tort} —fraction of material with tortuosity smaller than t	Ideally, charges should have straight paths to the relevant electrode

- A-material connected to cathode, and the useful fraction, f_{out}^{conn} , of both materials. This individual quantification helps to identify potential bottlenecks to charge transport.
- The complementary nature of the process is quantified by the fraction, f_{out}^{path} , of interface for which paths to *both* electrodes exist.
 - To quantify length of paths to both electrodes, we compute the path length from the interface to the relevant electrodes, d^e and d^h .
 - To further quantify length of paths, we compute the tortuosity of paths, t . Tortuosity is the ratio between the path length to the relevant electrode through BHJ, and ideal straight path length to the electrode without any constraints. Tortuosity is computed for domains that are connected to relevant electrode.

Table I provides a comprehensive, hierarchical set of morphology descriptors that quantify each stage of the photovoltaic process.²⁷ We noticed that the calculation of each of these descriptors can be simplified to two basic concepts: identifying distinct components in the morphology, and computing distances between two points in the morphology. This naturally resulted in representing the discretized morphology as a labeled, weighted, undirected graph and using efficient graph based algorithms to construct these descriptors. This procedure is detailed in Sec. III.

III. METHOD

We utilize fast algorithms from graph theory^{21,22} (specifically depth-first search for connected components, and Dijkstra's algorithm for distances) to construct the morphology descriptors.

In the first step, we represent a discretized morphology as a labeled, weighted, undirected graph. We represent each pixel/voxel of the image as a vertex in the graph, and we assign a label (here, a color) representing each type of mate-

rial: donor (black) or acceptor (white). We assume that appropriate thresholding is performed to get a binary image. In our approach, we assume that interface between A-material and D-material is sharp. The local neighborhood information is used to create edges that connect each vertex with its first- and second-order neighbors. Each edge is weighted according to the physical distance between the two vertices.

In the second step, we query this graph to compute the descriptors. All morphology descriptors reduce to three basic algorithmic constructs: finding connectivity between regions, selecting specific regions, and finding shortest paths within these regions. We provide more details including the algorithm outlines in the supplementary information.²⁸

The complete framework is implemented in C using the boost library.²³ Run time for 2D data sets of size $\sim 500 \times 100$ vertices is, on average, 2 s on a Intel Xeon Quad 2 GHz computer with 12 GB of RAM. Run time for 3D data set of size ~ 5.5 million voxels is 15 min on the same machine.

IV. RESULTS AND DISCUSSION

We interrogate two types of BHJ morphologies. The first is a transmission electron microscopy (TEM) cross section image taken from Moon *et al.*,¹³ while the second one is a 3D BHJ obtained from numerical modeling of the fabrication process.^{24,25} The TEM cross section image of BHJ taken from Moon *et al.*¹³ consists of a BHJ fabricated using a Poly(3-hexylthiophene) (P3HT) and Phenyl-C61-butyric acid methyl ester (PCBM) blend. Figure 1(a) shows the two-phase representation of the TEM image, where black regions represent A-material (PCBM-rich domain), and white regions represent D-material (P3HT-rich domain). This image consists of 1060×106 pixels (1 pixel corresponds to 1 nm). We note that this image represents a two-dimensional average of a three-dimensional structure (across the thin slice). But we argue that Moon *et al.* have shown minimal variability of the morphology by changing the thickness of

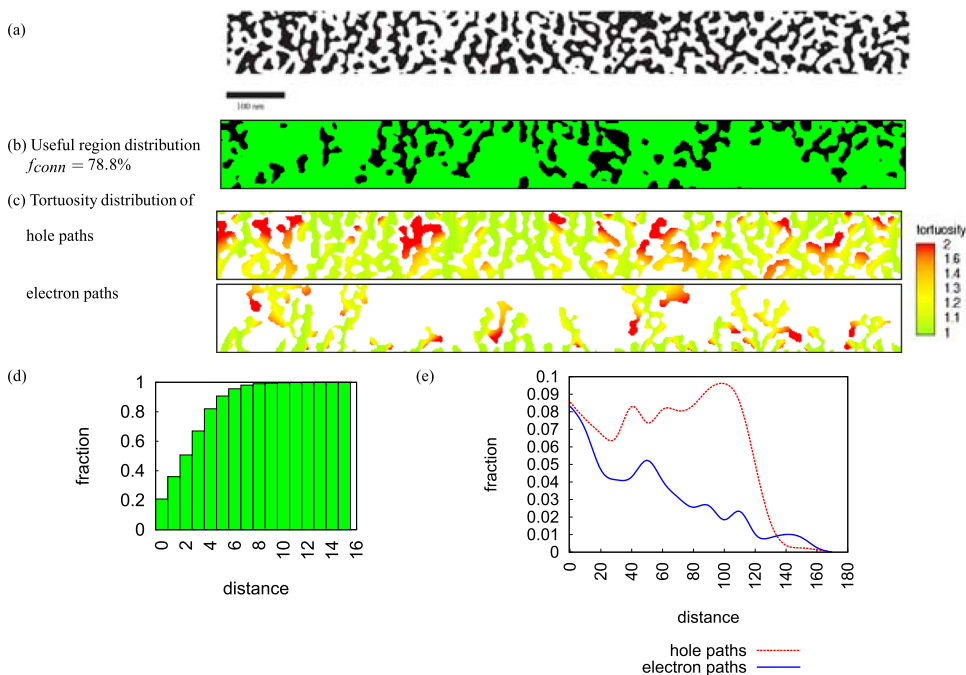


FIG. 1. (a) The two-phase representation of the TEM image of BHJ-morphology, taken from Ref. 13. (b) Distribution of useful regions. (c) Distribution of tortuosity of hole paths and electron paths. Morphology characterization: (d) distance distribution of D-material to the interface, visualized as a cumulative histogram, and (e) distance distribution of paths from interface to electrodes.

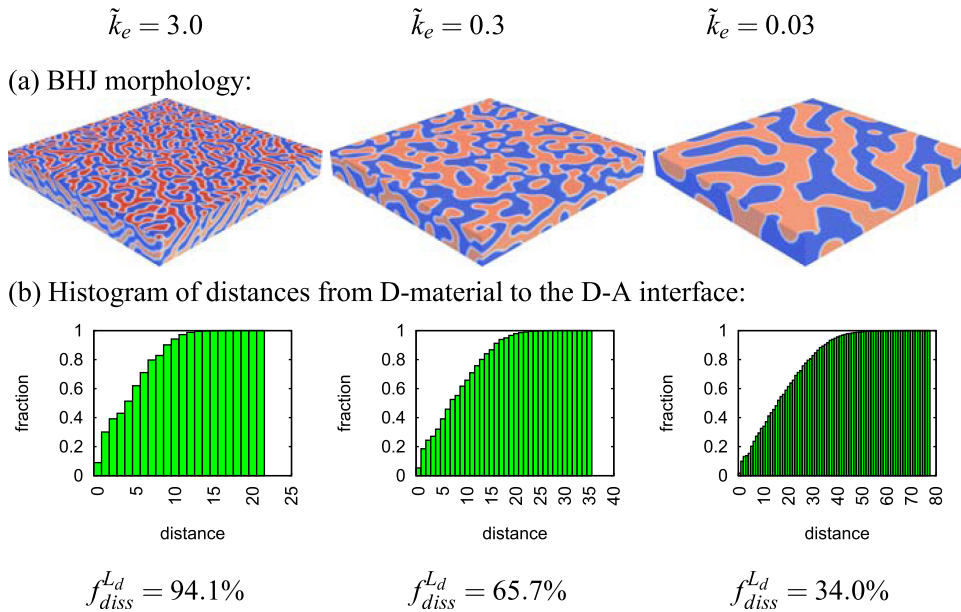


FIG. 2. Characterization of the two-phase representation of the 3D BHJ-morphology for three evaporation rates: \tilde{k}_e . (a) BHJ-morphology, (b) histogram of distances from D-material to the interface and extracted values of D-material fraction with distance to the interface shorter than $L_d = 10$ nm.

the slice and, hence, this is a reasonable representation of the morphology. We also analyze three 3D BHJ morphologies obtained computationally for three different evaporation rates.²⁵ Figure 2(a) depicts the 3D BHJ for three evaporation rates. Each morphology has dimensions $810 \times 810 \times 100$ nm³. This choice of BHJs allows us to demonstrate the universality of our method (2D vs 3D, experimental vs computational).

We concentrate on two types of investigation: First, we identify the bottlenecks in performance by characterizing BHJ with respect to each photovoltaic subprocess. This part is particularly important, because it allows for step-by-step analysis of the morphology and potentially provides valuable insight into linking structure and property. Next, we identify whether the given morphology is more efficient in a traditional configuration, or an inverted configuration. Apart from detailed characterization of BHJ, the developed framework allows us to probe several approaches for efficiency enhancement. For example, we can perform virtual characterization to test if traditional or inverted architecture is better. For typi-

cal OSCs fabricated on ITO substrates, traditional architecture is the one in which ITO is the anode.

A. Analysis of 2D TEM image of BHJ

Detailed characterization of this morphology is summarized in Table II. We first look at light absorption descriptors. The morphology consists of 58.2% of photo active material (f_{abs}). By weighting with the light intensity variation across the depth¹⁷ (and its reflection from bottom electrode), the effective fraction of thin film that absorbs light (to generate excitons) increases to 163.8% (f_{w-abs}).

Next, we look at exciton dissociation descriptors. The cumulative histogram of distances from D-material to the D-A interface is shown in Figure 1(d). The fraction of D-material whose distance to the D-A interface is shorter than exciton diffusion length ($L_d = 10$ nm) is 99%. In fact, only 1% of D-material lies between 10 nm and 16 nm to the D-A interface. The weighted fraction of D-material is $f_{w-diss} = 78.6\%$ (Table II).

Finally, we look at charge transport descriptors. Half (53.6%) of A-material is not connected to the cathode, while almost all D-material is connected to the anode (97%). Considering connectivity of both A- and D-material to respective electrodes reveals that only 79% of the photoactive layer is useful for charge transport. The low connectivity of A-material to the cathode affects charge transport and is clearly seen when we construct an interface-based descriptor. Only 46% of the D-A interface, f_{out}^{path} , has paths to both electrodes via corresponding materials. However, it is important to note that since this is only a 2D slice of the active layer, this low connectivity may be only an ‘‘artifact’’ of the 2D representation.

Quantifying the tortuosity of the morphology (of both electron-donor and electron-acceptor regions) is of particular interest due to the finite life time of charges and effect of electric field. We quantify the quality of paths by determining the shortest path that charges need to travel from the D-A interface to each electrodes. This is evaluated for each point on the *useful interface*. On an average, electrons travel a distance of

TABLE II. Detailed characterization of TEM image for two configurations: traditional and inverted, with respect to all subprocesses of photovoltaic process.

	Traditional	Inverted
f_{abs} (%)	58.2	58.2
f_{w-abs} (%)	163.8	163.3
$f_{diss}^{L_d}$, $L_d = 10$ nm (%)	99.4	99.4
f_{w-diss} (%)	78.6	78.6
I	13 499 nm	13 499 nm
f_{out}^{conn} (%)	78.8	80.83
f_{conn}^D, f_{conn}^A (%)	96.9, 53.6	96.4, 59.0
f_{out}^{path} (%)	45.9	50.0
f_{tor1}^D, f_{tor1}^A , $t = 1$ (%)	19.8, 19.9	18.8, 25.9
f_{tor1}^D, f_{tor1}^A , $t \leq 2$ (%)	93.6, 95.4	94.6, 89.9
Average path length: d^h (nm)	66.9	66.6
Average path length: d^e (nm)	52.9	60.8

53 nm to reach the cathode, while holes travel a distance of 67 nm to reach the anode. The distance data are further used to construct two histograms depicting path lengths: through A-material to cathode and through D-material to anode. Comparing both histograms (Figure 1(e)) allows us to assess the degree of path balance of the morphology.

To quantify the quality of paths, we compute the tortuosity of D-material and A-material with connection to the relevant electrode. We plot the distribution of tortuosity in Figure 1(c). We mark paths of tortuosity one ($t = 1$) with color green (straight paths), regions with tortuosity larger than 2 with red color, and intermediate tortuosity with yellow color. We analyze tortuosity of useful hole paths and electron paths individually. 19.8% of the useful D-region has straight paths to anode, while useful A-material consists of 19.9% of regions with straight paths to cathode. Regions with tortuosity one constitute ideal paths—that have no obstacles. Analysis of tortuosity distribution can also be used to identify and quantify dead ends and cul-de-sacs, i.e., domains with large tortuosity. Charges traveling through these regions can be easily trapped and eventually recombine. In the analyzed morphology, D-material consists of 6.4% of regions with tortuosity larger than 2, while A-material consists of as much as 4.6% of domains with high tortuosity.

Regions of large tortuosity together with domains that have no connection to the relevant electrode have minimal chance to contribute to charge transport. In the analyzed morphology, 9% of D-domain and as much as 49% of A-domain satisfy this condition.

Finally, we compare two configurations, traditional and inverted. It is often advocated⁵ that an inverted configuration gives higher efficiencies. We switch between configurations by simply flipping the morphology (Figure 1(a)) about the horizontal axis. All morphology descriptors for both configurations are shown in Table II. We notice no significant difference in descriptors of each stage of the photovoltaic effect. However, morphology descriptors used to characterize both configurations are marginally better for inverted configuration. In particular, the length of paths is better balanced, and a larger fraction of interface has complementary paths to both electrode (by 4%).

B. Analysis of 3D BHJ

In Table III, we include detailed characterization of three 3D-BHJ. All three morphologies are interpenetrated morphologies with perfect connection to the relevant electrodes. All descriptors reflecting the connectivity of domains to electrodes ($f_{conn}^A, f_{conn}^D, f_{conn}^{path}, f_{out}^{path}$) are optimal, i.e., 100%, for all three morphologies. In such cases, the entire morphology is useful with respect to charge transport. However, evaporation rate affects the quality of paths. The higher the evaporation rate, more tortuous the paths to relevant electrode. For example, examination of D-path tortuosity reveals that for the first morphology ($\tilde{k}_e = 3$, the highest evaporation rate) only 15% of the paths are straight paths (tortuosity $t = 1$) to the electrode. In contrast, the third morphology ($\tilde{k}_e = 0.03$, the lowest evaporation rate) consists of 72% of straight paths. Similarly, the fraction of straight paths for A-material

TABLE III. Detailed characterization of 3D BHJ morphology with respect to all subprocesses of photovoltaic phenomena ($L_d = 10$ nm).

	$\tilde{k}_e = 3$	$\tilde{k}_e = 0.3$	$\tilde{k}_e = 0.03$
f_{abs} (%)	57	54	52
f_{w-abs} (%)	136.4	129.6	124.3
$f_{diss}^{L_d}$ (%)	94.1	65.7	34.0
f_{w-diss} (%)	67.3	52.1	31.1
f_{out}^{conn} (%)	100	100	100
f_{out}^{path} (%)	100	100	100
$f_{tort}^D, f_{tort}^A, t = 1$ (%)	15.2, 14.8	33.2, 32.3	71.7, 72.2
$f_{tort}^D, f_{tort}^A, t \leq 2$ (%)	100, 100	100, 100	100, 100
	Path length		
Hole d^h (nm)	59.1	60.9	55.3
Electron d^e (nm)	70.2	61.9	56.3

decreases with evaporation rate. This is because for lower evaporation rate, morphology has more time to evolve and coarsen, creating more bulky domains with less tortuous domains. Less torturous morphologies also show higher potential for balanced paths. The difference in average path length between hole and electron is only 1 nm, while for more torturous BHJ this difference increases to 10 nm.

Better charge transport properties for less torturous BHJ come, however, with a price of larger domains. Larger domains have worse properties with respect to exciton dissociation. In particular, the domains whose size is larger than twice the exciton dissociation length cannot contribute fully to exciton dissociation. This tendency is reflected in the exciton dissociation descriptors. For the highest investigated evaporation rates (Figure 2 left), 94% of D-material is distributed within L_d distance to the interface. In contrast, for the lowest evaporation rate, this quantity decreases to 34%.

Light absorption characteristics are similar for all three morphologies as the blend-ratio is the same across these three morphologies.

The main difference between these three 3D-BHJs is the trade-off between charge transport and exciton dissociation. Coarser BHJ has less torturous domains but domains larger than exciton diffusion length. Finer morphologies have more curly paths but smaller domains compatible with exciton diffusion length.

V. CONCLUSIONS

It is clear that understanding the role of morphology is of great importance for OSCs due to its intricate effect on the final efficiency of the device. A key challenge hindering quantitative comparison of complex BHJ morphologies is the lack of physically meaningful and easily computable morphology descriptors. In this work, we have formulated a set of morphology descriptors that reflect the complex multistage nature of photovoltaic process. The morphology descriptors are constructed in hierarchical way, focusing on each stage of photovoltaic process. We performed detailed quantification of two types of representative morphologies with respect to all subprocesses of photovoltaic effect. We reduced a complex 2D/3D BHJ morphology to a set of physically

meaningful parameters enabling quantitative comparison between morphologies. In particular, we quantitatively compared inverted and traditional device configurations. We were also able to identify bottlenecks in the analyzed morphologies. This framework opens up the possibility of data-driven and high-throughput analysis of process-structure-property relationships by reducing large data-sets of morphologies into tractable sets of numbers. Such a graph-based framework, furthermore, naturally allows extensions to incorporate the effects of crystallinity, anisotropy, and multiple phases. We also envision broad applicability of this strategy to other areas involving transport in heterogeneous structures, such as percolation pathways in geomechanics, porous media, and drug release from polymeric membranes.

ACKNOWLEDGMENTS

S.T. was supported in part by NSF-0831903. S.C. acknowledges financial support from Iowa Power Fund, provided by state of Iowa's Office of Energy Independence. B.G. and O.W. are supported in part by NSF PHY-0941576, NSF CCF-0917202, and a NSF-1149365 (CAREER).

- ¹G. Yu, J. Hummelen, F. Wudl, and A. J. Heeger, "Polymer photovoltaic cells: Enhanced efficiencies via a network of internal donor-acceptor heterojunctions," *Science* **270**, 1789–1791 (1995).
- ²S. H. Park, A. Roy, S. Beaupre, S. Cho, N. Coates, J. S. Moon, D. Moses, M. Leclerc, K. Lee, and A. J. Heeger, "Bulk heterojunction solar cells with internal quantum efficiency approaching 100%," *Nature Photon.* **3**, 297–302 (2009).
- ³S. Peumans, P. Uchida, and S. R. Forrest, "Efficient bulk heterojunction photovoltaic cells using small-molecular-weight organic thin films," *Nature* **425**, 158–162 (2003).
- ⁴H. Hoppe and N. S. Sariciftci, "Morphology of polymer/fullerene bulk heterojunction solar cells," *J. Mater. Chem.* **16**, 45–61 (2006).
- ⁵L. Chen, Z. Hong, G. Li, and Y. Yang, "Recent progress in polymer solar cells: Manipulation of polymer:fullerene morphology and the formation of efficient inverted polymer solar cells," *Adv. Mater.* **21**, 1434–1449 (2009).
- ⁶S. von Bavel, E. Sourty, G. de With, and J. Loos, "Three-dimensional nanoscale organization of bulk heterojunction polymer solar cells," *Nano Lett.* **9**, 507–513 (2009).
- ⁷M. Pfannmoller, H. Flugge, G. Benner, I. Wacker, C. Sommer, M. Hanselmann, S. Schmale, H. Schmidt, F. A. Hamprecht, T. Rabe, W. Kowalsky, and R. R. Schroder, "Visualizing a homogeneous blend in bulk heterojunction polymer solar cells by analytical electron microscopy," *Nano Lett.* **11**, 3099–3107 (2011).
- ⁸G. Buxton and N. Clarke, "Predicting structure and property relations in polymeric photovoltaic devices," *Phys. Rev. B* **74**, 085207 (2006).
- ⁹A. C. Mayer, M. F. Toney, S. R. Scully, J. Rivnay, C. J. Brabec, M. Scharber, M. Koppe, M. Heeney, I. McCulloch, and M. D. McGehee, "Bimolecular crystals of fullerenes in conjugated polymers and the implications of molecular mixing for solar cells," *Adv. Funct. Mater.* **19**, 1173–1179 (2009).
- ¹⁰L. Hou, E. Wang, J. Bergqvist, B. V. Andersson, Z. Wang, C. Miller, M. Campoy-Quiles, M. R. Andersson, F. Zhang, and O. Ingans, "Lateral phase separation gradients in spin-coated thin films of high-performance polymer: Fullerene photovoltaic blends," *Adv. Funct. Mater.* **21**, 3169–3175 (2011).
- ¹¹B. Ray, P. R. Nair, and M. A. Alam, "Annealing dependent performance of organic bulk-heterojunction solar cells: A theoretical perspective," *Sol. Energy Mater. Sol. Cells* **95**, 3287–3294 (2011).
- ¹²W. Ma, C. Yang, and A. J. Heeger, "Spatial fourier-transform analysis of the morphology of bulk heterojunction materials used in "plastic" solar cells," *Adv. Mater.* **19**, 1387–1390 (2007).
- ¹³J. S. Moon, J. K. Lee, S. Cho, J. Byun, and A. J. Heeger, "Columnlike" structure of the cross-sectional morphology of bulk heterojunction materials," *Nano Lett.* **9**, 230–234 (2009).
- ¹⁴B. Lei, Y. Yao, A. Kumar, Y. Yang, and V. Ozolins, "Quantifying the relation between the morphology and performance of polymer solar cells using Monte Carlo simulations," *J. Appl. Phys.* **104**, 024504 (2008).
- ¹⁵L. Meng, Y. Shang, Q. Li, Y. Li, X. Zhan, Z. Shuai, R. G. E. Kimber, and A. B. Walker, "Dynamic monte carlo simulation for highly efficient polymer blend photovoltaics," *J. Phys. Chem. B* **114**, 36–41 (2010).
- ¹⁶S. von Bavel, E. Sourty, G. de With, K. Frolic, and J. Loos, "Relation between photoactive layer thickness, 3D morphology, and device performance in P3HT/PCBM bulk-heterojunction solar cells," *Macromolecules* **42**, 7396–7403 (2009).
- ¹⁷F. Monestier, J. Simon, P. Torchio, L. Escoubas, F. Flory, S. Bailly, R. Debettignies, S. Guillerez, and C. Defranoux, "Modeling the short-circuit current density of polymer solar cells based on P3HT:PCBM blend," *Sol. Energy Mater. Sol. Cells* **91**, 405–410 (2007).
- ¹⁸L. Pettersson, L. Roman, and O. Inganas, "Modeling photocurrent action spectra of photovoltaic devices based on organic thin films," *J. Appl. Phys.* **86**, 487 (1999).
- ¹⁹L. Onsager, "Initial recombination of ions," *Phys. Rev.* **54**, 554–557 (1938).
- ²⁰B. Ray and M. A. Alam, "A compact physical model for morphology induced intrinsic degradation of organic bulk heterojunction solar cell," *Appl. Phys. Lett.* **99**, 033303 (2011).
- ²¹T. H. Cormen, C. E. Leiserson, R. L. Rivest, and C. Stein, *Introduction to Algorithms* (MIT, 2009).
- ²²E. W. Dijkstra, "A note on two problems in connexion with graphs," *Numer. Math.* **1**, 269–271 (1959).
- ²³See <http://www.boost.org/> for "Boost library," (2011).
- ²⁴O. Wodo and B. Ganapathysubramanian, "Computationally efficient solution to the Cahn–Hilliard equation: Adaptive implicit time schemes, mesh sensitivity analysis and the 3D isoperimetric problem," *J. Comput. Phys.* **230**, 6037–6060 (2011).
- ²⁵O. Wodo and B. Ganapathysubramanian, "Modeling morphology evolution during solvent-based fabrication of organic solar cells," *Comput. Mater. Sci.* **55**, 113–126 (2012).
- ²⁶This is currently accepted portrait of the morphology. Recent studies suggest that there may be third phase being a mixture of D and A.⁷ The third phase, however, can be easily taken into account in this framework.
- ²⁷It is interesting to note that some of these constraints conflict with each other. For instance, long interface and short paths are mutually exclusive (for non-fractal surfaces).
- ²⁸See supplementary material at <http://dx.doi.org/10.1063/1.4752864> for (a) a brief description of the equivalence between morphology and graph, and (b) a sketch of algorithms used to quantify morphology.